6-9-2016

Crack Tip Micromaching by Femtosecond Laser for Fracture Testing of Metal Laminates

Ricardo Martin Martinez

Ricardo M. Martinez
Candidate

Mechanical Engineering
Department

This thesis is approved, and it is acceptable in quality and form for publication:

Approved by the Thesis Committee:

Dr. Yu-Lin Shen , Chairperson

Dr. Mehran Tehrani

Quinn McCulloch

Crack Tip Micromachining by Femtosecond Laser for Fracture Testing of Metal Laminates

by

Ricardo M. Martinez

B.S, Mechanical Engineering, University of New Mexico, 2011

Thesis

Submitted in Partial Fulfillment of the

Requirements for the Degree of

Master of Science
Mechanical Engineering

The University of New Mexico

Albuquerque, New Mexico

May, 2016

Dedication

To my mother, father, & step-father for a lifetime's worth of love & encouragement.

To my brothers and sisters who've had my back through thick & thin.

To my nieces and nephews: Always move forward!

Love you all!

Acknowledgements

I would like to thank everyone who contributed to this work. First and foremost, my LANL mentor Quinn McCulloch from whom I've learned so much and whose input on this project has been invaluable. Also, my UNM advisor Dr. Yu-Lin Shen for serving as my thesis advisor and who has been essential to this research and patiently given me direction. Dr. Nate Mara of LANL who provided the materials for this research and whose expertise is greatly appreciated. Dr. Anatoly Efimov and Dr. Steve Gilbertson, both of LANL, for their beam characterization guidance. Dr. Mehran Tehrani who served on my graduate committee. Again, thank you all for your guidance and contribution to this research project. This would not have been possible without you.

Crack Tip Micromachining by Femtosecond Laser for Fracture Testing of Metal Laminates

by

Ricardo M. Martinez

B.S, Mechanical Engineering, University of New Mexico, 2011

M.S., Mechanical Engineering, University of New Mexico, 2016

Abstract

This thesis presents an experimental study of the effects of ultrafast laser ablation on the mechanical properties of metal laminates followed by FEA simulation to elucidate future experimental potential. The metals investigated are copper, niobium, and copper/niobium accumulative roll bonded (ARB) laminates. The two laminate materials in this study have a nominal layer thickness of 1.8 microns and 65 nanometers; the effects of the laser processing on the ARB materials are characterized in the rolling direction as well as the transverse direction as the material exhibits anisotropic properties. The aforementioned materials are examined via scanning electron microscopy and energy dispersive spectroscopy techniques to obtain changes in layer restructuring and modification. The motivation of this study is to characterize the heat affected zone in the materials produced by ultrafast laser processing to determine whether ultrafast laser ablation is a viable method for creating artificial cracks for SEM in-situ mini cantilever fracture testing. A parameter space is defined to attempt to capture an acceptable set of laser settings which both reduce the heat affected zone and create an etched geometry mimicking a crack into the sample to facilitate crack propagation in bend testing. Finally, simulation is performed using ANSYS to determine sample geometry constraints induced by both the laser-notched crack tip's geometry and the limitations of the experimental

apparatus used for in-situ testing. Additionally, simulations will provide insight into the plastic behavior of the layered structure.

Contents

List of Figures

List of Tables

Chapter 1

Introduction

1.1 Lasers

The term laser is an acronym for the light amplification by stimulated emission of radiation. The first operational laser was created in 1960 [1]; this set the foundation for the development of continuous wave and pulsed lasers which eventually led to the progression to fast and ultrafast lasers currently used in various scientific and commercial applications. The focus of this manuscript is on ultrafast laser interactions with metals, namely copper and niobium, with the goal of determining whether it is a viable method for ablating artificial crack tips for fracture testing. Ultrafast lasers are those in which the pulse duration is on the order of tens of femtoseconds to sub-picosecond. This regime presents the need for new governing equations to describe energy transport phenomena associated with light-matter interactions at such a short time scale. The extremely short pulse duration which can last for less than a millionth of a billionth of a second ablates matter in a mostly athermal manner. Attributed to this fact, is that the photon-matter interactions produce a minimalized heat affected zone during ablation as compared to continuous wave, microsecond, nanosecond, and picosecond pulsed lasers. This characteristic has opened the door to many micro- and nano-etching/ablation processes referred to as laser beam machining (LBM).

In metals, which are the focus of this study, this ultrafast phenomenon occurs when the energy transferred to electrons is subsequently transferred to the lattice via electron-phonon coupling. This causes the atoms to pass quickly through the liquid phase directly to the gas phase before the energy can transfer to the lattice through diffusion, thereby minimizing heat propagation and its

effects on surrounding material. Once the energy is imparted to the electrons from the incident photons, energy transfer from the free electrons to the lattice is regulated by the electron-phonon coupling factor which is a material property that varies from metal to metal.

1.2 Governing Equations

1.2.1 Ultrafast laser-metal energy transport

Although this is not a theoretical study of energy transport, it is necessary to understand the mathematical models describing short time-scale light matter interactions. In this section a brief overview of the evolution of light-matter, namely light-metal, interaction phenomena will be presented to elucidate the uniqueness of ultrafast laser-metal interactions. This uniqueness is with respect to energy transport in the femtosecond time regime. In addition, it highlights the challenge of precisely micromachining metal laminates consisting of non-uniform layers with constituent materials having vastly different material properties relevant to ultrafast energy transport mechanisms.

The principles governing laser-metal interactions have evolved from a simple model using the Fourier heat conduction as a foundation, in the case of continuous wave (CW) lasers, to more complex mathematically vigorous models. Continuous wave laser interaction with metals is described using the Fourier model of heat conduction also known as the parabolic one-step (POS) model [2, 3].

$$C\frac{\partial T}{\partial t} = \nabla \cdot (k\nabla T) + S$$

where T is the temperature, t the time, C the volumetric heat capacity, k the thermal conductivity, and S is the laser heating source term. This model makes

two key assumptions: energy transfer occurs instantaneously and that it is a diffusive process. While this model has proven to be one of the best models in mathematical physics, it's been shown via transient heat-conduction boundary-value problems that temperatures vary initially then converge to nearly identical profiles after a time on the order-of-magnitude of the relaxation time of the material's electrons [4]. In other words, a pulse of heat at one location in a medium causes an instantaneous change in temperature at some distant location, a physical impossibility. Thus, a more accurate model was required to account for finite speed propagation.

It was proposed that heat transfer has a wave-type nature and propagates at a finite speed rather than a diffusive process occurring at infinite speed [4, 5]. The product of this approach was the hyperbolic one step (HOS) model, also known as the relaxation model, for heat transfer, which included the addition of a heat-flux relaxation term, $\tau,$ to the Fourier heat conduction model.

$$C\frac{\partial T}{\partial t} = -\nabla \cdot \boldsymbol{Q} + S$$

$$\tau\frac{\partial \boldsymbol{Q}}{\partial t} + k\nabla T + \boldsymbol{Q} = 0$$

where $\boldsymbol{Q}$ is the heat flux through the metal and τ is the relaxation time for free electrons in a metal. The relaxation time, $\tau,$ is a characteristic time for the average of a distribution of electrons in a solid to achieve equilibrium after an external disturbance has been removed [6]. It was shown that this model was not a valid extension of the parabolic one step model at very short timescales when the pulse duration is much greater than the thermalization time of the material [7, 2]. Furthermore, it has been demonstrated mathematically that a negative temperature field occurs under particular conditions in violation of the second law of thermodynamics [8].

Next, it was proposed that energy transfer from photons to internal energy or lattice vibration is not instantaneous. Rather, it occurs through a two-step

energy-deposition process [9]. First, radiant energy is transferred to the free electrons in the metal. Second, the energy imparted on the electrons transfers to the metal lattice or phonons with the rate of transfer mediated by an electron-phonon coupling factor. The parabolic two-step model (PTS) that emerged from this approach is treated with the assumption that the electron temperature and lattice temperature can be characterized by T_e and T_l, respectively.

$$C_e(T_e)\frac{\partial T_e}{\partial t} = \nabla \cdot (k\nabla T_e) - G(T_e - T_l) + S$$

$$C_l(T_l)\frac{\partial T_l}{\partial t} = G(T_e - T_l)$$

where the subscripts e and l represent the properties of the electrons and lattice, respectively. S Remains a laser source term, and G is the electron-phonon coupling term, which indicates how rapidly energy is transferred from the electrons to the lattice and can be expressed as:

$$G = \frac{\pi^2 m_e n_e {u_s}^2}{6 t_c(T_e) T_e}$$

where m_e, n_e, u_s, t_c, and T_e are the electron mass, electron number density, speed of sound, electron mean free time between collisions at temperature T_e, and the electron temperature, respectively [10].

Property	Copper	Niobium
Thermal Conductivity, k, (W/ m-K)	386.01	51.93
Electron-Phonon Coupling Factor, G, (10^{16} W/m^3-K)	4.8 ± 0.7	387 ± 36

Table 1.1: Thermal Conductivity,k, and Electron-phonon coupling factor, G, of Cu and Nb [11]

The drawback of the PTS model are that a particular solution for the femtosecond time regime can only be readily formulated for intensities that are

linear functions of time and that it was not rigorously derived from the Boltzman transport equations for electrons as performed by Qiu *et al.* [9, 12, 2]. Additionally, energy transport is predicted to propagate at an infinite speed contrary to observations [13]. The electron temperature in the post-hundred femtosecond to sub-picosecond time range was validated by comparing equilibrium thermodynamics with the measured electron distribution function [14, 15]. The flaws become an issue only when the pulse duration is less than a few hundred femtoseconds; shorter than this and the electron temperature is only approximate. This model applies to the current study, as the pulse width is approximately 780 fs.

In the case of pulses with a duration of less than a few hundred femtoseconds, the hyperbolic two-step model as derived by Qiu and Tien is the appropriate mathematical description of energy transport [2]. The final formulation describing photon-metal energy transport is the dual hyperbolic two-step model, which varies from the standard PTS by accounting for energy transport in both the electrons and lattice rather than by the electrons alone. There will be no further elaboration on these models as they are not applicable to the current study due to the relatively long pulse width of the laser and the material properties of copper and niobium.

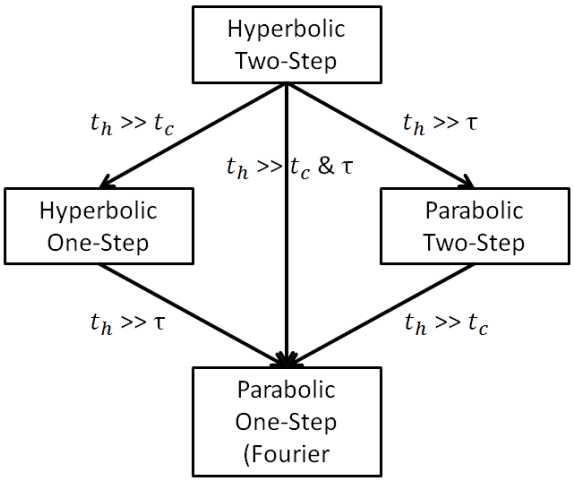

Figure 1.1: Interrelationship between laser heating models [2]

The above schematic depicts the selection process for the appropriate heating models for light-metal interactions depending on three characteristic times. The thermalization time, electron relaxation time, and heating time, t_h, which is the laser pulse duration [2]. For the laser used for this thesis, the pulse duration was measured using autocorrelation and found to have a temporal width of approximately 780 fs at full-width half max assuming a temporally Gaussian intensity profile (see Appendix 1). Adhering to the flow of the schematic, copper's heat transfer is governed by the parabolic two-step model due to long thermalization time and short electron relaxation time. On the other hand, niobium's heat transfer mechanism is governed by the traditional Fourier conduction model as its thermalization and relaxation are both much shorter than the pulse duration; at least one and order and two orders of magnitude, respectively. Taking this discrepancy into account, the lowest possible laser fluence is used to minimize the heat affected zone while exploiting the incubation effect, which is discussed in section 1.2.3, to further reduce the necessary fluence required for material ablation.

Property	Copper	Niobium
Thermalization t_c (fs)	600	50
Electron Relaxation τ (fs)	30	4

Table 1.2: Thermalization and Electron Relaxation times of copper and niobium at room temperature [12]

1.2.2 Gaussian Beam Intensity Profile

The laser used in this experiment is a Raydiance Smart Light with a spatially Gaussian intensity profile described by

$$I(x,y) = I_0 e^{\left[-\frac{2(x-x_o)^2}{\omega_x^2} - \frac{2(y-y_0)^2}{\omega_y^2}\right]}$$

where $I(x,y)$ denotes beam intensity at some location relative to the central axis of the beam where the maximum intensity is located at $I_0(x_0,y_0)$ along the axis of beam propagation. Furthermore, ω_x and ω_y are the $\frac{1}{e^2}$ half-widths in the x and y directions, respectively [16]. The spot size of the focused laser beam is characterized by ω_x and ω_y in which a certain amount of the beam's Gaussian profile is captured. There are multiple accepted criteria for defining a Gaussian spot size [17]. In this study, the $\frac{1}{e^2}$ criterion is used to measure the spot size to calculate and compare with previous studies the laser irradiation fluence on the sample to remain near the damage threshold of the material and, thereby, reduce the heat affected region and collateral damage.

The knife edge method was used to measure the effective spot size in order to dial in the desired energy per pulse. This method requires scanning a razor blade across the beam at the machining plane and recording the measured power. The data is then differentiated with respect to position using the algorithm described by [18]

$$\frac{dP_T}{dx} = \frac{1}{2}\left(\frac{y_{i+1} - y_i}{x_{i+1} - x_i} + \frac{y_i - y_{i-1}}{x_i - x_{i-1}}\right)$$

This series of measurements and calculations were performed in both the x- and y-directions to calculate the Gaussian spots sizes to determine whether any substantial astigmatism existed in beam profile. The data for this process can be found in the appendix. The results from this show that the values of ω_x and ω_y are 2.25 um and 3 um, respectively.

1.2.3 Incubation Effect

The single shot ablation threshold of a metal is the energy per area (fluence) at which material removal is initiated. This single shot threshold fluence is a function of the materials thermal and dynamical properties [19]. The

threshold fluence, however, decreases as more pulses are applied to the same location. This phenomenon is known as the incubation effect wherein the materials threshold fluence lowers as a function of applied pulses. Although current research has proposed several different contributions to the incubation effect, a comprehensive mechanism has not yet been established [20]. Currently, proposed contributors to the incubation effect are heat accumulation at high laser pulse repetition rates, plastic deformation accumulations due to induced thermal stress fields, increased energy absorption due to surface roughening, and decreased energy penetration depth [21, 22, 23, 24].

Mathematically the incubation effect can be represented using a power law as given by

$$\phi_{th}(N) = \phi_{th}(1)N^{S-1}$$

where $\phi_{th}(N)$, $\phi_{th}(1)$, N, and S are the threshold fluence for N pulses, one pulse, the number of pulses N, and the incubation coefficient S, Respectively [25].

1.3 Goals of Study

The motivation of this study is to create a high aspect ratio ablated trench with a sharp leading edge to simulate a crack into a metal laminate to facilitate mechanical testing for fracture characterization. Benefits of ultrafast laser machining are that it is readily accessible, ablates features quickly, and affords the ability to be selective about crack placement. Focused ion beam (FIB) has been used along with the currently used ultrafast laser in another study for artificial notching, but said study investigated the fracture toughness along the constituent materials' interface [25]. The unique aspects of the laser machining, in this case, is that the laser processing is perpendicular to the direction of the layers and that the layer thicknesses reported are an average where single layer thickness has been seen to be as large as 10um in the case of the nominally 1.8um layered sample. This layer non-uniformity amplifies the difference in

material properties on the ablation dynamics. The tradeoff between FIB and laser notching is that FIB has a much higher spatial resolution at the expense of processing time. A 25um deep notches can be micro machined across a 250um length in a few minutes whereas similar notches via FIB took up to 8 hours [26]. Also, FIB tends to modify samples through ion implantation which could prove consequential in small scale testing [27].

The final portion of this research will provide a modeling aspect using ANSYS to investigate the plastic zone ahead of a crack during deformation to show whether linear elastic fracture mechanics applies to future mechanical testing and what geometric constraints must be met to facilitate future experiments determined by equipment capabilities and sample fabrication limitations.

Chapter 2

Laser Parameterization

2.1 Experimental Setup

This experiment uses a Raydiance Smart Lite ultrafast laser with a fundamental wavelength of 1552nm and pulse width of 833fs. The laser is frequency doubled so that the wavelength is 776nm using a Beta Barium Borate (BBO) crystal. Due to this modification of the beam, the pulse width is measured as described above using autocorrelation and found to have a pulse width of 780fs after frequency doubling. The ability to attenuate the laser beam is achieved via a Polarizing Beam Splitting Cube (PBSC) in series with Half-Wave Plate (HWP). The beam is turned to follow a path that strikes the samples being studied in normal incidence. The beam is focused through an M Plan Apo NIR 20X focusing objective with laser focusing achieved by adjusting the Z height of the focusing objective relative to the sample surface via a Newport MFA-CC miniature linear stage. A dielectric mirror allows for simultaneously imaging with a CCD camera while laser ablation is taking place. Once the sample is in focus beneath the laser, its translation in the X and Y plane is controlled by Newport XMS 180 and XMS 50 ultra-precision linear motor stages, respectively. A beam sampler is used to monitor power throughput after the attenuating region. In this experiment, the repetition of the laser was set to 2kHz to avoid heat accumulation.

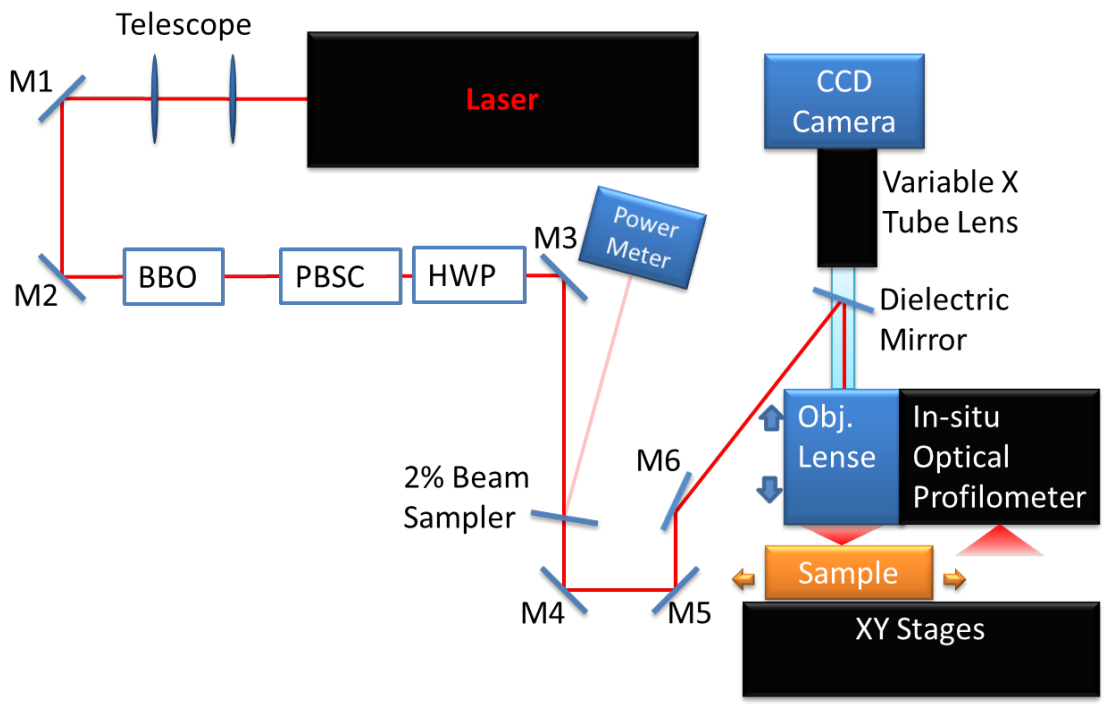

Figure 2.1: Raydiance Laser Micro-Machining Diagram

2.2 Sample Compendium

The samples tested are annealed copper, niobium, and copper/niobium micro- and nano- laminates created through an accumulative roll-bonding (ARB) process in which the materials undergo Severe Plastic Deformation (SPD). The initial Nb and Cu materials used to manufacture these samples are reactor grade Nb (99.97%, ATI Wah Chang) and oxide-free high conductivity Cu (99.99% pure, Southern Copper and Supply). The ARB process for the laminate material in this study starts with a copper clad first-rolling where a full niobium sheet is sandwiched between two half sheets of copper and put through a rolling mill. Further details regarding sample preparation and treatments can be found in reference [28]. Samples investigated here are pure Cu, Nb, 1.8um nominally layered Cu/Nb, and 60nm nominally layered Cu/Nb. Both the 1.8um and 60nm ARB laminate materials will be examined in both the rolling and transverse directions relative to the rolling process.

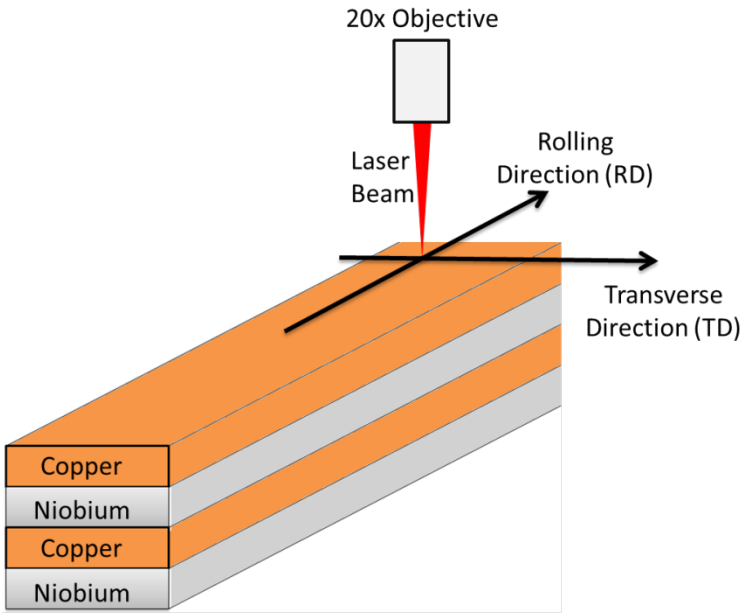

Figure 2.2: Accumalive roll bonded copper/niobium laminate sample orientation relative to laser processing

Before laser processing, all of the samples' top and side surfaces received polishing via Allied High Tech diamond lapping films. The resulting surface roughness reported in the following table are measured with a Bruker DektakXT stylus profilometer. The values are for the top surfaces which are the focus of the laser processing. The roughness increases from lowest value of pure materials to the largest layered laminates; this is inferred to be attributed to the polishing rates of the constituent materials differing from each other, which is amplified as the layers become thicker.

	Cu	NB	60nm RD	60nm TD	1.8um RD	1.8um TD
RMS (nm)	39.50	43.99	72.56	55.11	289.45	325.26
Average (nm)	49.78	34.99	63.20	67.40	356.60	294.72

Table 2.1 Top surface roughness measurements for samples after polishing and prior to laser processing

2.3 Laser Processing Parameter Space & Results

The single shot ablation threshold fluence of copper has been shown to be three times as high as that of niobium while their incubation coefficients are nearly identical [21]. With this in mind, the first set of experiments set out to utilize incubation at an exceptionally large number of overlapping pulses while remaining at just above the lowest reported ablation threshold of copper which is nearly coincident with previous experiment's threshold fluence of 0.02 $\mu J/cm^2$. The ablation threshold of copper has been reported to fall between 0.018 $\mu J/cm^2$ to 1.4 $\mu J/cm^2$ depending on the ablation regime, the initial surface conditions concerning roughness and reflectivity, and the wavelength of the laser used [29]. Two ablation regimes have been shown to exist for copper exposed to sub-picosecond laser pulses [30]. These regimes display a sharp contrast between ablation rates of material and their ranges become apparent when plotted logarithmically. In the gentle, or optical skin depth regime, material is removed at a slower rate. In the hard, or effective heat penetration regime, material is ablated at a greater rate. In the case of copper, the gentle regime is at fluences less than 0.5 $\mu J/cm^2$ while the hard regime occurs at fluences greater than 0.7 $\mu J/cm^2$. In between these two regimes is a transitional region that is not well defined. This two regime phenomena is pulse-width independent but exists only for sub-picosecond pulses. There exist large amounts of research regarding copper/ultrafast laser interactions due to its wide use. Niobium, however, has not received nearly as much attention in this respect, so the majority of the decision making process in this study are directed by the data and studies performed on copper.

2.3.1 Low-Fluence Incubation Reliant

Based on prior experiments performed with the Raydiance laser on these particular samples it's been shown that surface modification of copper can be

seen at fluences as low as 0.02 μJ/cm^2. This fluence is achieved via beam attenuation and coincides with previously reported threshold fluence. Also, no change in surface texture is observed with further attenuation.

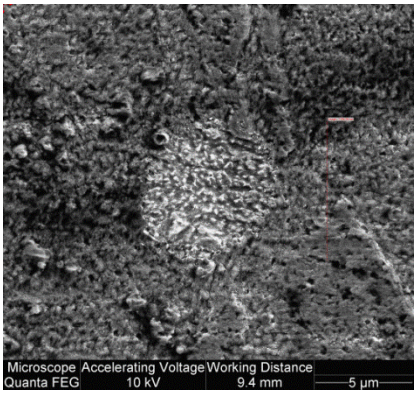

Figure 2.3: Single Shot Feature on Cu at 0.02 μJ/cm2

This low fluence was chosen initially with the idea that incubation would increase material ablation rates at moderate to tremendous amounts of overlapping pulses, thus ablating both the copper and niobium layers with minimal energy. All samples had the same array of features machined. Seven features are machined into each sample with sufficient spacing, approximately 50ums, to isolate each feature. The seven cuts are straight lines machined onto the sample's top surface leading off of one edge so that the effects on the layered structure can be examined from a cross-sectional point of view. These cuts vary only by the amount of overlapping pulses, which are controlled by the stages' translational velocity. The overlapping pulses in this set of experiments were chosen as 100, 400, 1K, 4K, 10K, 20k, and 50k. At this fluence, SEM micrographs show that material is not ablated efficiently. At the lowest amount of overlapping pulses (OLP), only a very shallow trench is created. At the largest number of applied pulses, 50k, the material is melted and re-solidified in the channel. This trend reveals that as the number of applied pulses is increased, material is not effectively ablated. Rather, as the number of pulses increases, only the depth of the heat affected zone increases.

The following micrographs are focused on the top corner of the samples. The orientation of the micrographs is meant to capture both the relative ablation morphology along the top surface as well as the accompanying effect on the layered structure. Polishing of the top and side surfaces resulted in a corner radius where the two meet. This radiused corner is present on all samples and more pronounced on some samples than others. Additionally, it should be noted that since the layers are not perfectly distributed, both copper and niobium bands can be seen on the top surface of the sample. The micrographs are 50/50 mixes of secondary electrons and back-scattered electrons to expose both topographical and elemental variations.

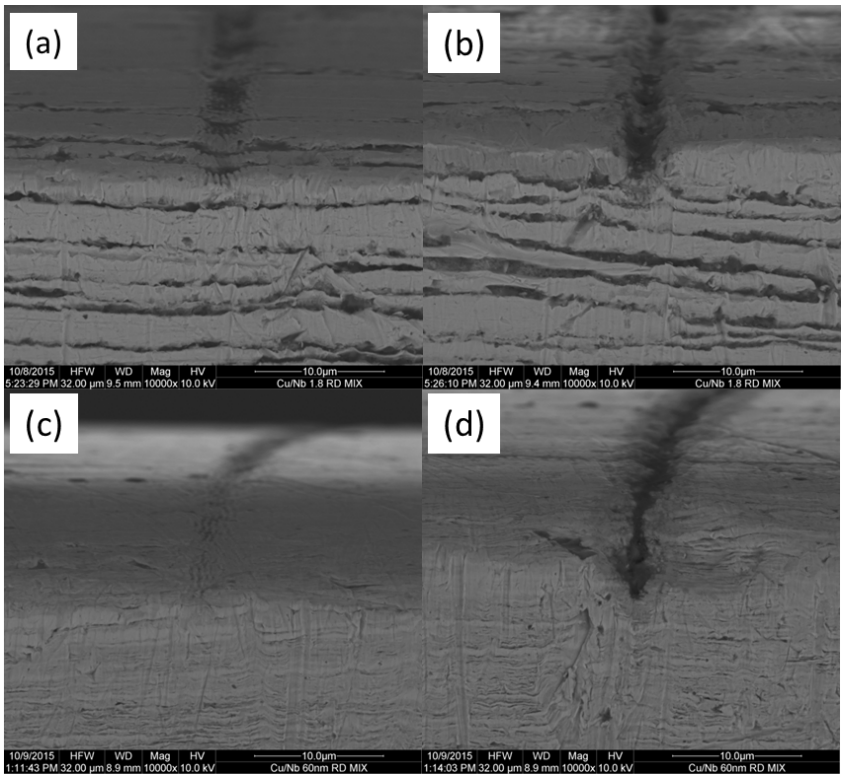

Figure 2.4: SEM Secondary Electron / Backscatter Electron micrographs of (a) 100 OLP on 1.8 um RD, (b) 50k OLP on 1.8 um RD, (c) 100 OLP on 60 nm RD, (d) 50k OLP on 60 nm RD

2.3.2 Moderate-Fluence Incubation Reliant

The next iteration involves increasing the energy while remaining within the gentle ablation regime. The fluence chosen is 0.5 µJ/cm^2 while repeating the above sets of tests cuts to take advantage of the incubation effect. The effects can be seen below. As the number of applied pulses is increased, a larger heat affected zone begins to develop in both the 1.8um and 60nm layered material. This trend noticeably declines as fewer pulses are applied. Furthermore, as applied pulses increases, material is not efficiently ejected from the trench, rather it redeposits.

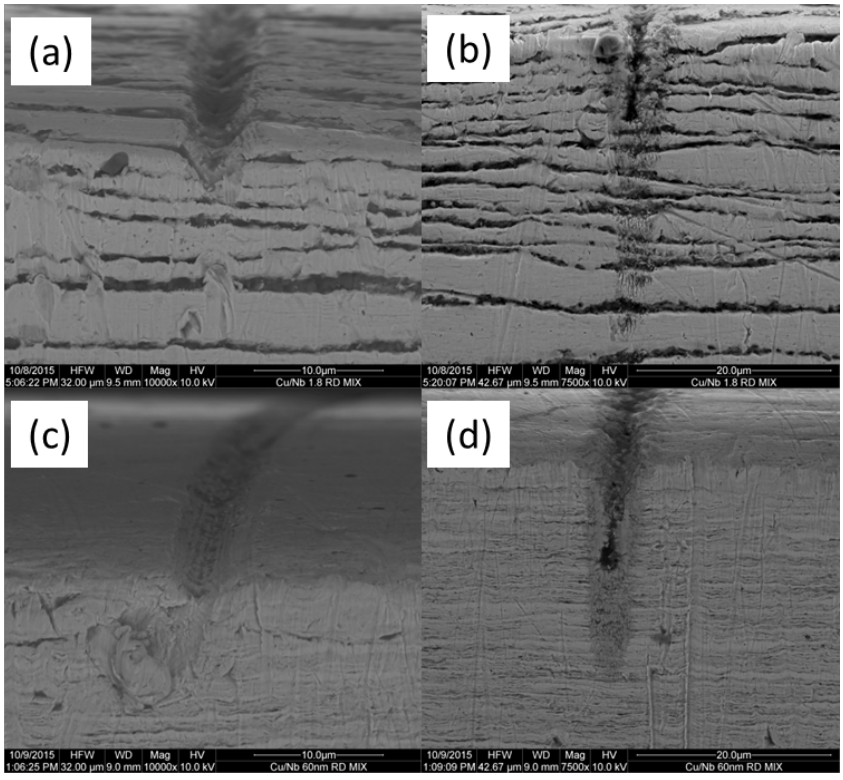

Figure 2.5: SEM Secondary Electron / Backscatter Electron micrographs of (a) 100 OLP on 1.8 um RD, (b) 50k OLP on 1.8 um RD, (c) 100 OLP on 60 nm RD, (d) 50k OLP on 60 nm RD

The following figure contains an SEM micrograph of the region of a 1.8um layered sample, which is processed at 0.5 µJ/cm^2 and 100 overlapping pulses. Since the trend of intermixing increases as the number of pulses increases, this

sample was examined via energy dispersive spectroscopy to evaluate the disruption of the layered structure. The circled region in micrograph (a) is the focus of the EDS scan performed in (c). This region shows that that the copper and niobium layers again become discrete.

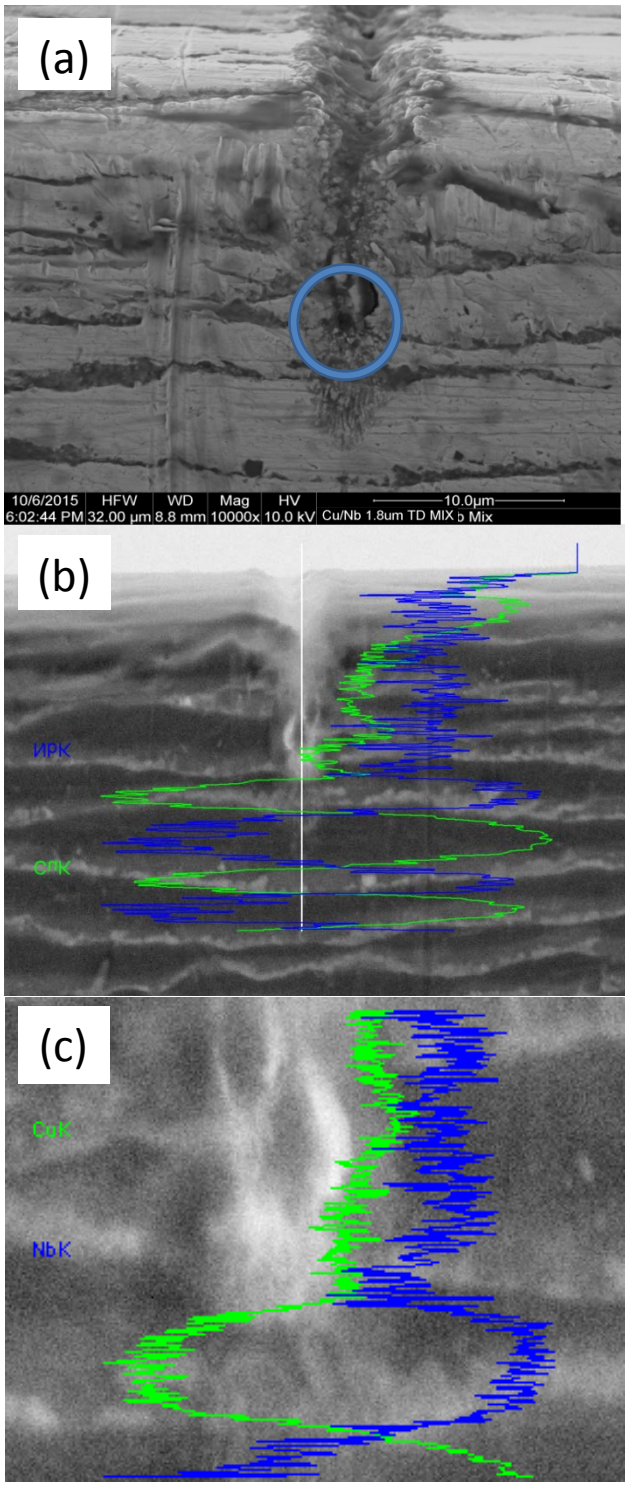

Figure 2.6: 1.8 um nominally layered Cu/Nb ARB laminate processed with 50k OLP shown in (a) SEM micrograph encompassing area of interest as inspected by (b) EDS results of scan along path indicated by white line and (c) EDS of laser machined tip highlighted with a blue circle in figure (a).

In the case of 100 overlapped pulses, a shallow trench was observed with no discernable intermixing or heat affects ahead of the laser processed zone, again, verified quantitatively via EDS and qualitatively via back scattered electron micrographs for the 1.8um layered material. Also, the ablated material is ejected from the channel rather than redepositing as was the result as the amount of applied pulses increased.

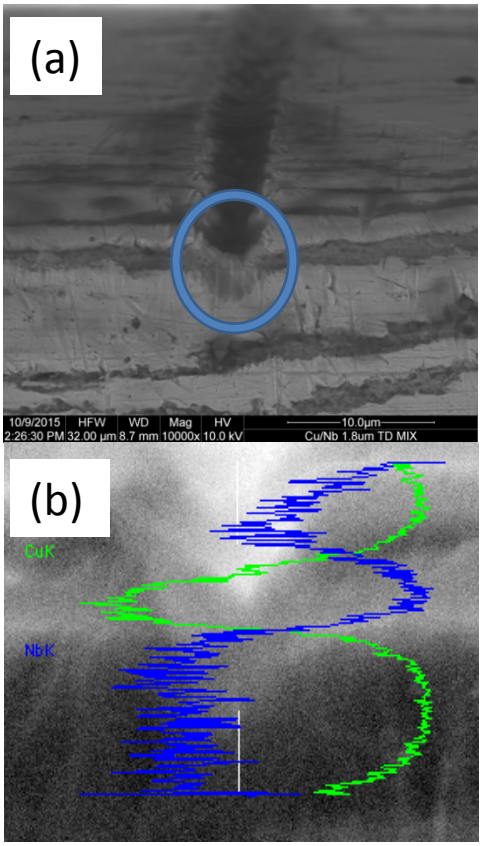

Figure 2.7: 1.8 um nominally layered Cu/Nb ARB laminate processed with 100 OLP. Shown in (a) SEM micrograph encompassing area of interest as inspected by (b) EDS results of scan performed along white line.

2.3.3 Moderate-Fluence Modified-Incubation

The final set of parameters chosen involves utilizing the incubation effect at the moderate fluence. However, overlapping pulses, which constitute the incubation, effect are applied by scanning the sample back and forth, so the laser

irradiates the same region during multiple successive passes. During the second experiment set, it’s shown that the heat affected zone decreased as the number of overlapping pulses decreased. This reduction led to the decision of choosing 10, 50, and 100 overlapping pulses while performing 1, 5, 10, and 20 consecutive passes for each number of overlapping pulses at different locations on the sample. The laser focus was not changed with respect to the sample during successive laser scans. Additionally, a gas nozzle was attached to the focusing objective to assist debris removal by directing a stream of compressed gas directly onto the processing region. Nitrogen was chosen as the purge gas to reduce oxidation during laser processing. The resulting trend indicates that, as expected, the depth increases as successive passes increase. The deepest channel is machined with 100 overlapping pulses and 20 successive passes. The micrograph below shows the progression of channel depth for 100 overlapping pulses for 1, 5, 10, and 20 successive passes.

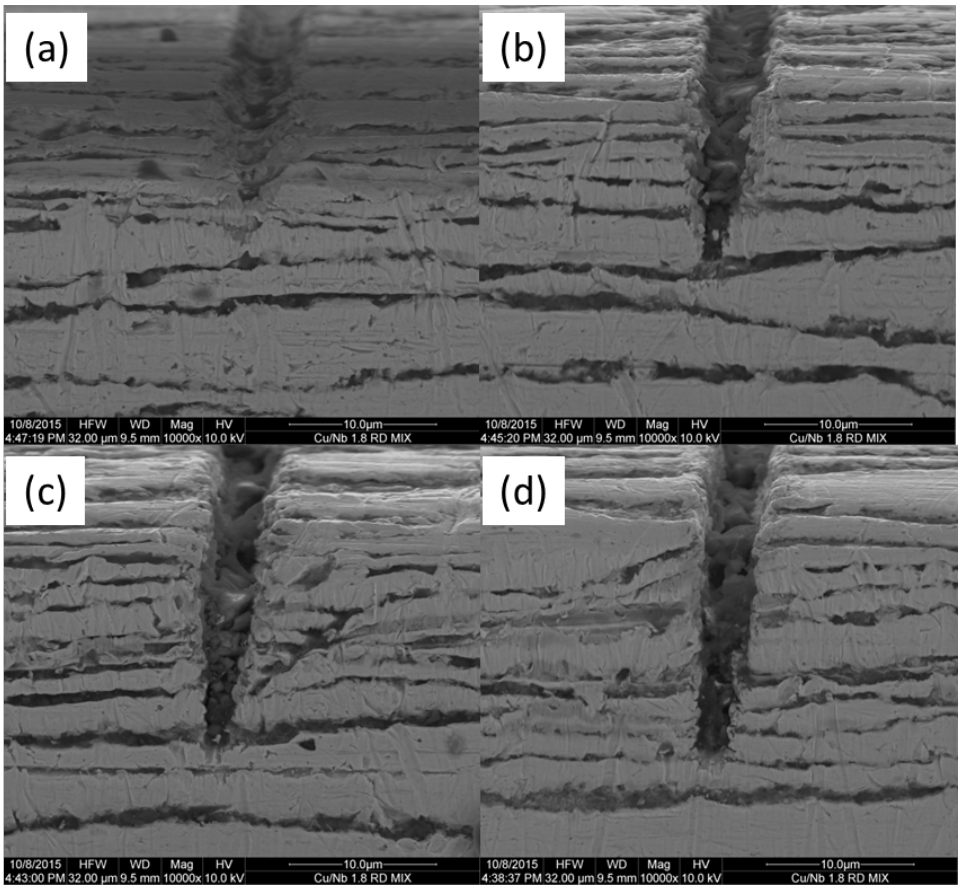

Figure 2.8: SEM micrographs of 1.8um rolled direction Cu/Nb laminate processed with 100 overlapping pulses at (a) 1 pass, (b) 5 passes, (c) 10 passes, and (d) 20 passes

Initially, the laser machined channels appear to be backfilled with ablated material, but following a 10-minute wash in a sonic bath in which the samples are submerged in ethanol the debris evacuated the trenches. This is the case for all channels made in the manner described in this section. Material redeposited from the methods described in 1.2.1 and 1.2.2 was verified to have remained in the machined features post-sonication.

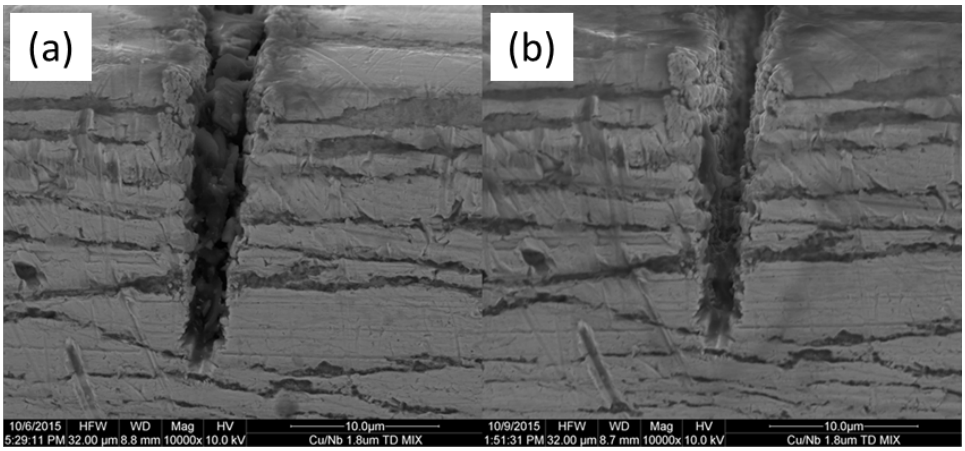

Figure 2.9: SEM micrograph of 1.8um rolled direction Cu/Nb laminate processed with 100 OLP at 20 successive passes (a) pre sonic bath and (b) post sonic bath.

Cut depth measurements are taken using Scandium XT post processing software and plotted for the pure annealed copper and niobium as well as the 1.8um and 60nm laminate materials in both the transverse and rolling directions. The resulting channel depths are presented for all materials in the following figure. One notable observation is that at lower number of passes there is a higher discrepancy in cut depth whereas the depths converge to much more consistent depths as the number of successive passes increases. This is particularly apparent in the case of 100 overlapping pulses where the channel depth at 20 passes falls between 18-19 microns. The results show that channel depth increases as a function of both increasing overlapping pulses and number of successive passes.

Finally, EDS scans show a reduction in the amount of oxygen present between samples processed via methods two and three. This is attributed to the uses of nitrogen as a purge gas. The scans in the following figure are performed along the vertical white line.

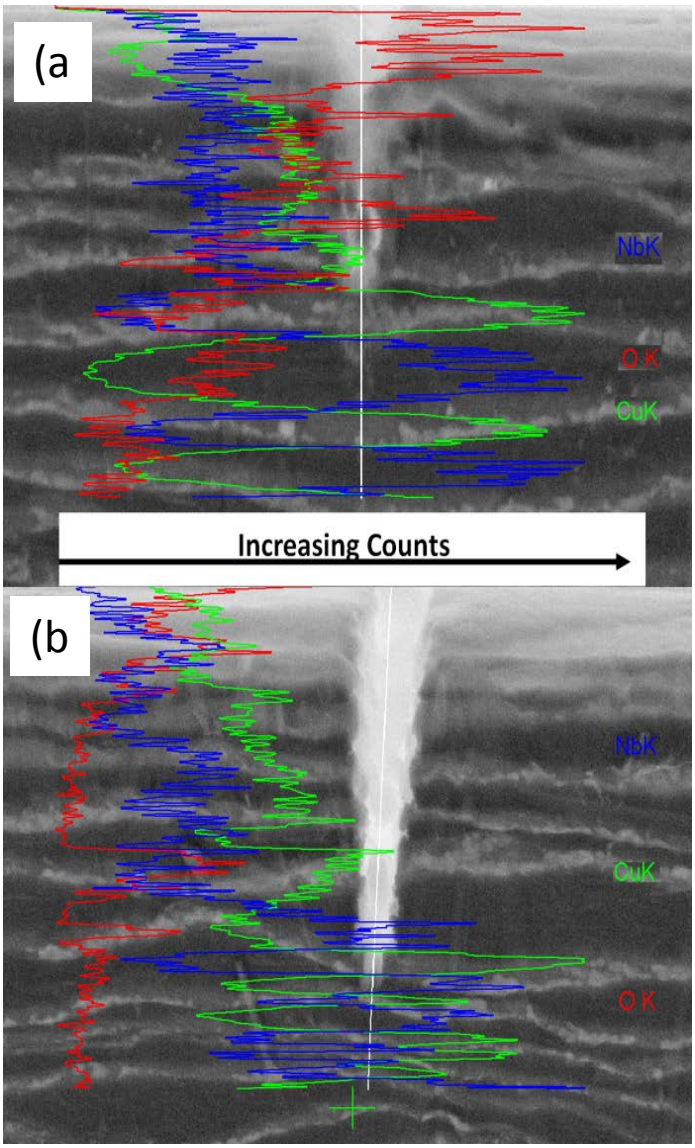

Figure 2.10: EDS results of (a) Method 2 ARB 1.8um ARB Cu/Nb laminate processed with 50k OLP and (b) : EDS results of (a) Method 3 ARB 1.8um Cu/Nb laminate processed with 100 OLP and 20 passes using nitrogen as a purge gas

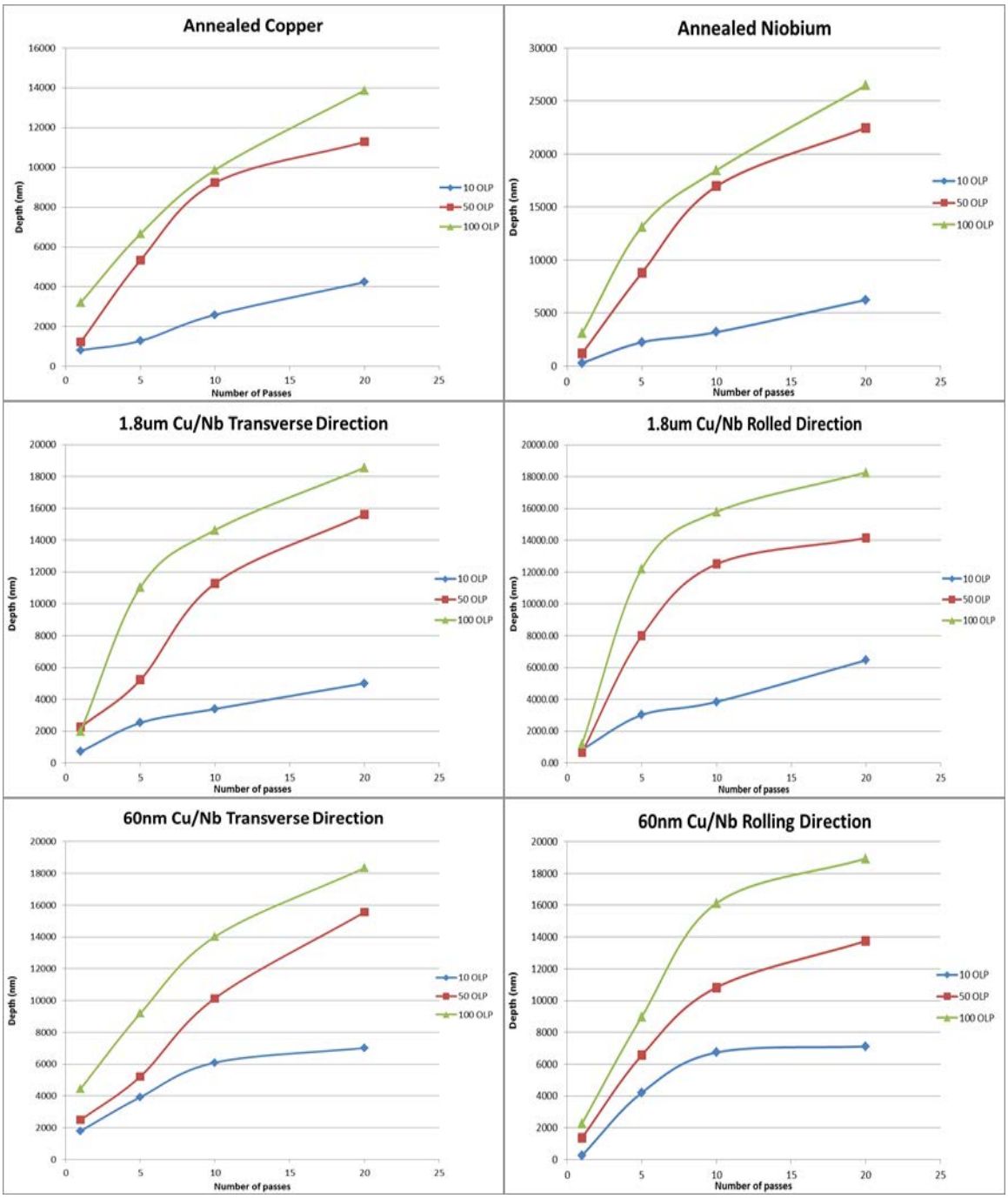

Figure 2.11: Depth measurements for each material for 10, 50, 100 overlapping pulses and 1, 5, 10, and 20 successive passes

2.4 Discussion

A systematic experimental approach to laser micromachining high aspect ratio trenches is performed in the preceding sections. Ultimately, channels with an aspect ratio of ~10:1 with a leading edge diameter of 1-2um are realized. The introduction of a gas-assisted modified-incubation technique is demonstrated to effectively machine artificial cracks in Cu/Nb ARB nano- and micro- laminates. The use of nitrogen as a processing gas reduced sample oxidation. Furthermore, using minimal energy and low laser pulse repetition rate, the heat effects are minimized.

There are a few interesting tendencies that should be considered. First, the leading edge of the successful laser machined trenches retains a consistent tip radius regardless of the cut depth. The trench only widens as successive passes are performed. Secondly, the depth of the trenches suggests an interesting trend. The depth of the channels cut into laminate materials, in the case of 100 overlapping pulses, very nearly matches the average cut depths of its constituents for the same number of passes. For instance, in the case of 100 overlapping pulses and 10 consecutive passes, the cut depth in copper and niobium are approximately 10um and 19um, respectively. The cut depths for both the 60nm and 1.8um laminate materials under the same parameter space fall between 14-16um.

Chapter 3

Simulation

The purpose of the simulation in this study is twofold: (1) establish the geometric limitations of the pillars based on fabrication and the in-situ testing limitations and (2) approximate the layered structure to observe the plastic behavior in the layers with respect to crack tip width. In both cases, simplifying assumptions are made. It is assumed that the materials have isotropic elasticity. Plastic behavior is treated as a bilinear isotropic hardening model having a constant tangent modulus, and hardening is treated as rate independent. The tangent modulus is estimated as the slope of the true stress-strain curve from the yield point to the ultimate tensile strength [31]. The layers are considered to be uniform and evenly distributed. The bulk Cu/Nb material properties are used in the simulation. The models are constructed in SOLIDWORKS and then transferred to ANSYS for 3-d simulation. The material properties and problem constraints are defined in ANSYS.

3.1 Bulk Model

In this section, single-material models are investigated. The material defined in this model is meant to mimic the Cu/Nb 60nm laminate material based on the bulk properties of the material [32]. The material's properties are taken from experimental data for the bulk Cu/Nb laminate material. Previous experiments on Cu/Nb ARB laminates have shown that as the layer thickness decreases, the strength of the material increases [32]. Also, for any particular layer thickness, the laminates show an increased strength in the transverse direction compared to the rolling direction. It is for this reason that the bulk model is based on the material properties of the 65nm layered material in the transverse direction. By simulating the most robust material, it ensures that the other

materials will also displace sufficiently when subject to the in-situ loading. Reference [32] is used to calculate the Young's and Tangent modulus of the bulk material. The Poisson ratio is calculated by the rule of mixtures. A table of material properties used in the layered simulation is included in that section of the study.

The SEM in-situ indenter available at the Los Alamos National Laboratory's Center for Integrated Nano Technology (LANL-CINT) has a maximum loading of 1N. The purpose of constructing a bulk model is to ensure that the loading capacity of the indenter is capable of deforming the pillars based on bulk properties. The mini-milling capability that will fabricate the pillars must also be taken into account. The achievable aspect ratio of pillars is 5:1 and the minimum cross-sectional dimensions are 50umx50um. Pillars with larger cross-sectional dimensions are ideal as pushing the limits of resolution can be testing. For this reason, three pillars at different size scales are modeled and their displacements are determined under a 1N load for two different notch dimensions; this results in 3 total geometries for both a 1um and 2um wide notch. The relative geometry is shown in the following figure.

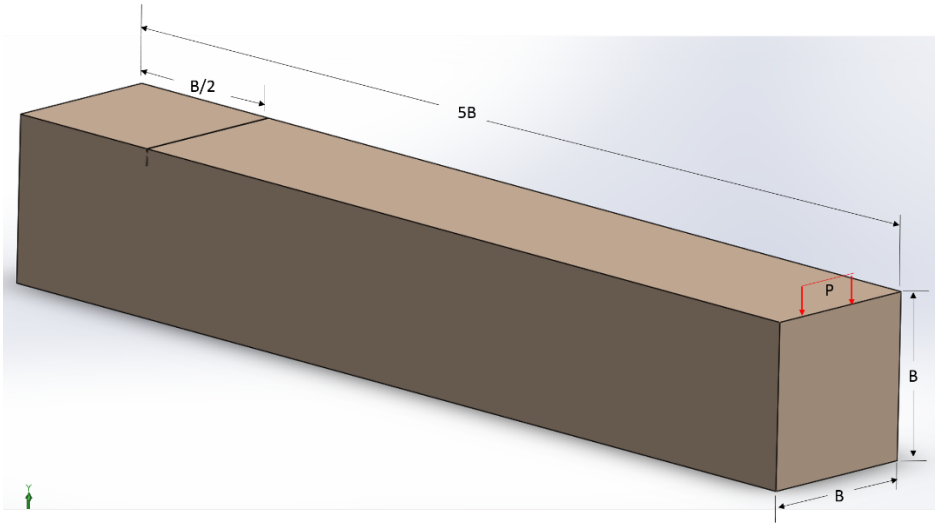

Figure 3.1: Bulk Model Geometry

The simulation is set up such that the beam is fixed at the face closest to the notch and the 1N load is applied along the edge denoted by P. B is chosen to

be 200um, 150um, and 100um. The experimental geometry and configuration are chosen based on previous cantilever experiments performed using the in-situ test equipment, which tested interfacial fracture behavior [26]. The notch is placed at B/2 away from the fixed end of the pillar.

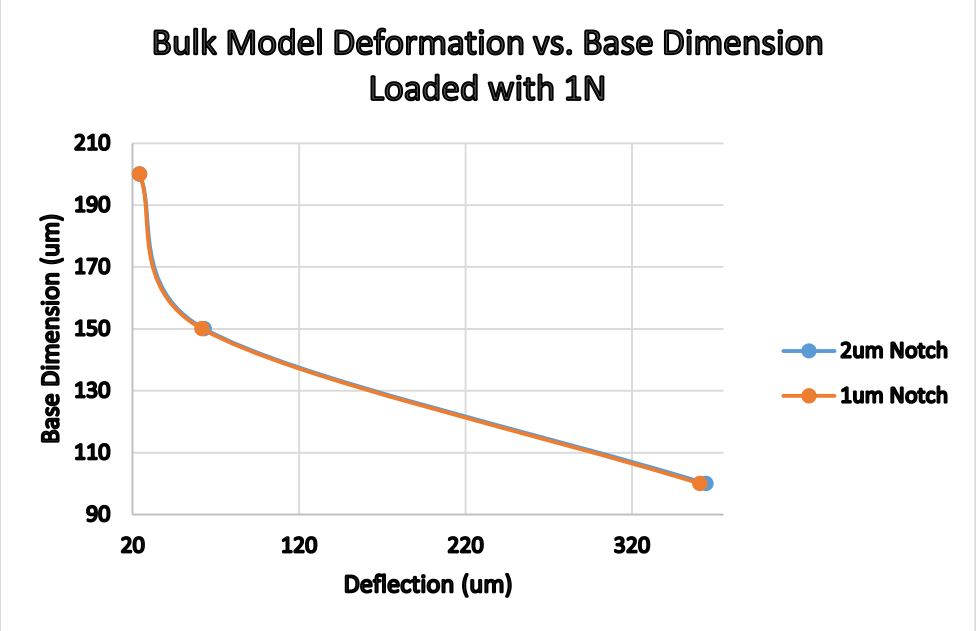

Figure 3.2. Bulk model deformation vs base dimension, B, for an applied load of 1N on 1um and 2um notched configurations.

Previous cantilever experiments performed at LANL-CINT characterizing Al/Zr interfacial bonding strength were loaded until a displacement equaling 70 percent of its base dimension were reached [26]. Pursuant to this, a base pillar dimension of approximately 140um corresponds to a resultant deflection of 100um or roughly 70 percent of the base value. The ramification is that pillars with dimensions of 140umx140umx700um, or less, should be fabricated for future tests to attain similar deflections to previous experiments. Another benefit is that it gives an upper limit, based on indenter capabilities, for sample fabrication. The model setup is validated through comparison of the analytical solution for a cantilever beam under loading and its associated deflection. The

percent error is approximately 1% for all bulk simulations as shown in appendix A3.

Qualitatively, it can be seen that intensity of the equivalent plastic strain increases as the notch tip width decreases as should be expected.

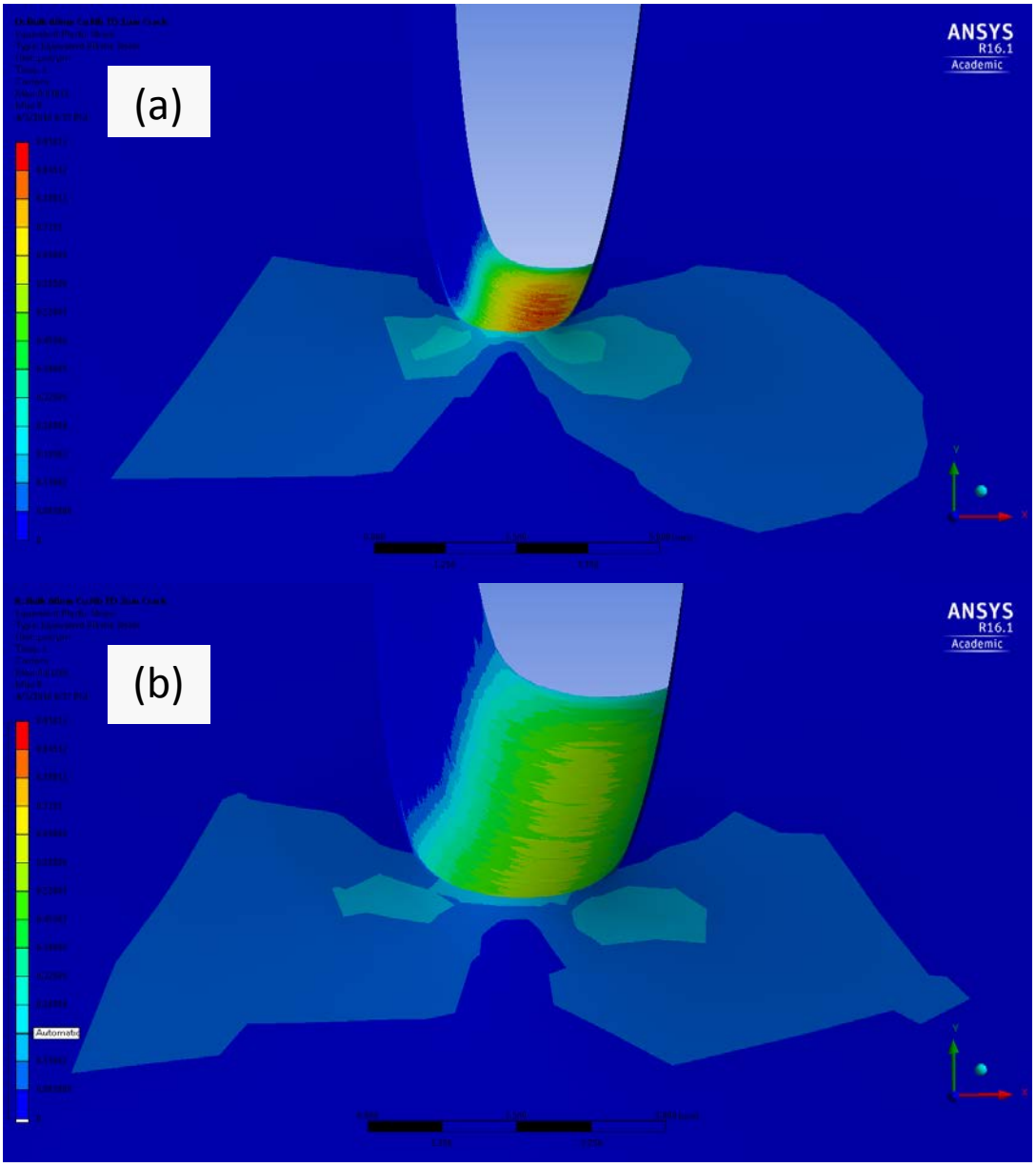

Figure 3.3 ANSYS simulation of plastic zone for bulk models with base length of 150um displaced by 1N load with a (a) 1um Notch and (b) 2um Notch.

3.2 Layered Model

The laminate material with a nominal layer thickness of 1.8um is considered in this section. This layer selection is due to ANSYS simulation constraints. As each layer is treated as a separate part in ANSYS, each layer receives its own set of elements, which are, at most, as tall as each individual layer. This layer thinning leads to a substantial growth in the number of elements beyond the computational capacity of the current ANSYS license. Furthermore, even with a layer thickness of 1.8um, the node/element limit of 256k was frequently exceeded during mesh refinement; this implored the use of lower quality elements away from the crack tip, which is the area of interest.

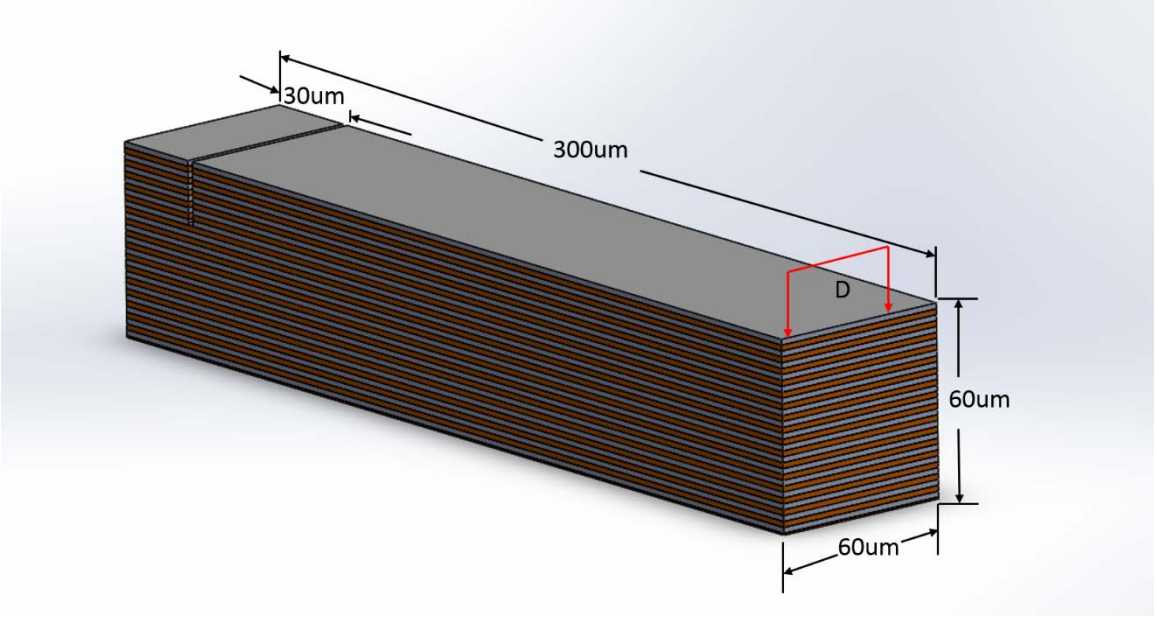

Figure 3.4. Layered Model Schematic

A 60umx60umx300um layered structure is modeled. An assembly of copper and niobium band-parts are created in SOLIDWORKS then imported to ANSYS. The ANSYS attachment between parts is selected as bonded. A single beam geometry is modeled in this set of simulations while the notch width is simulated at 1um and 2um. Again, this was due to simulation constraints. As each layer is treated as a separate part in ANSYS, the amount of nodes and

elements needed to model larger cantilevers grew substantially. Nevertheless, the geometry modeled is possible to fabricate for testing. The simulation was run with two different configurations: Once with a notch width of 1um and once with a notch width of 2um. This was done to show the effects of crack geometry on the plastic zone in the layers as effected by the notch width.

The material properties for the layers of the copper and niobium are derived from reported bulk material properties [33, 34, 35, 36, 37]. The simulation constraint for both models is the same: the face nearest the notch receives a fixed boundary condition. Rather than applying a load in this case, a displacement is applied along the edge of the pillar denoted by D. The displacement was chosen based on prior cantilever experiments [26]. The displacement was set to approximately 70% of the base dimensions of the pillar which, in this case, is 42um in the vertical direction. The material properties used in the layered study are listed in the table below.

	Young's Modulus	Poisson's Ratio	Yield Stress	Tangent Modulus
Copper	120 GPa	0.36	70 MPa	836.74 MPa
Niobium	105 GPa	0.40	206 MPa	1.589 GPa

Table 3.1 Material properties for multi-layered ANSYS simulations

In both the 1um and 2um channels, notch termination occurs in the copper layer. Additionally, the ANSYS simulation indicates a larger magnitude of equivalent plastic strain propagating through the copper layer for the 1um notch. The length and equivalent plastic strain scales are equal in the following figure for direct comparison. By comparison, it can be seen that a narrower notch leads to an increased equivalent plastic strain along the notch surface. Furthermore, a reduction of notch width is accompanied by a reduction in the propagation of the equivalent plastic strain through the copper layer.

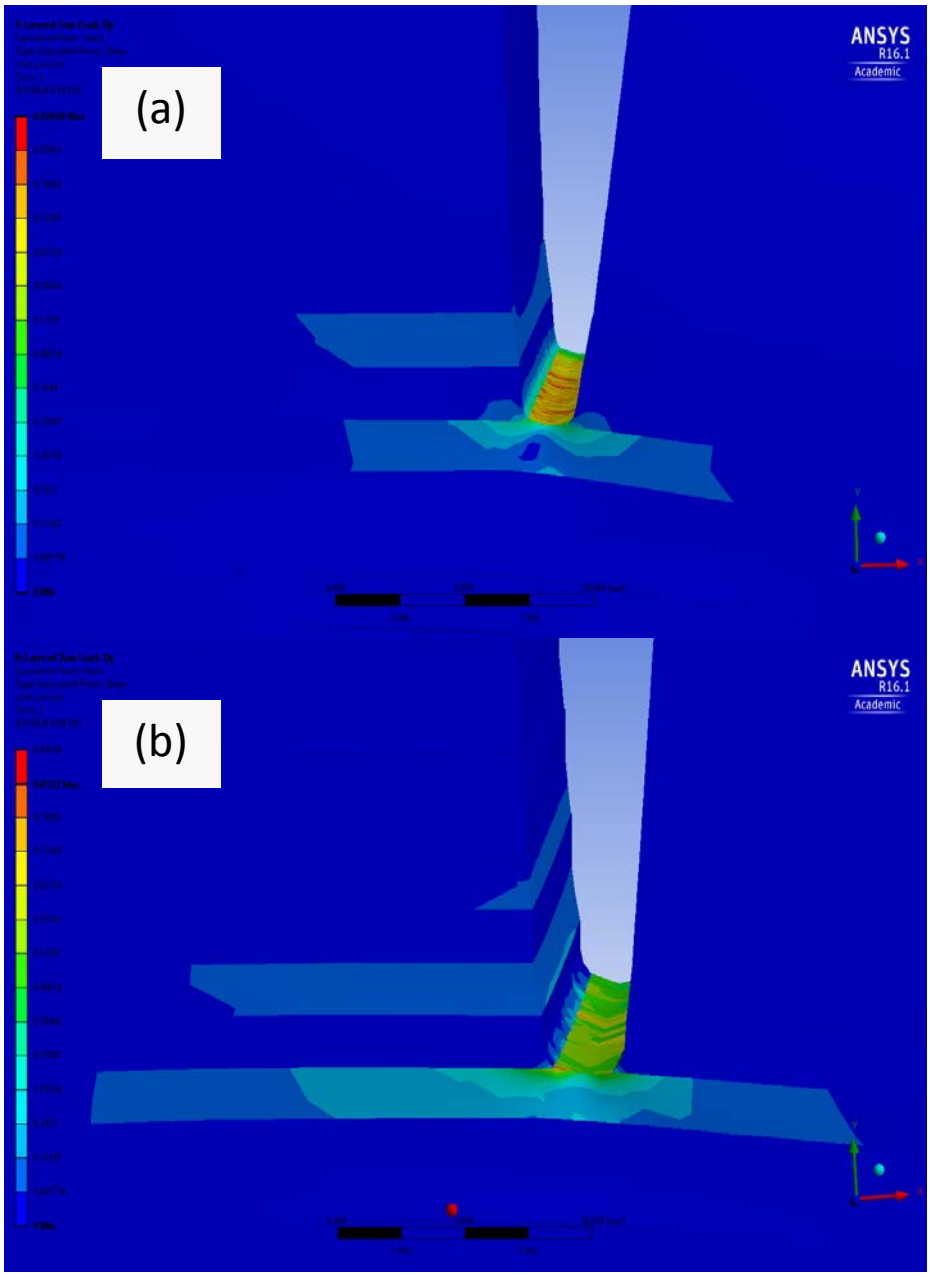

Figure 3.5 ANSYS equivalent plastic strain solution for 1.8um Cu/Nb model for (a) 1um and (b) 2um notch tip diameters. Larger equivalent plastic strain and crack tip termination occur in copper layer.

Chapter 4

Conclusions and Future Work

4.1 Conclusion

In this research, a systematic experimental method was applied to reveal a method of cutting high aspect ratio channels in copper and niobium accumulative roll bonded micro- and nano-laminates. The benefit of creating these channels, which act as artificial cracks, is that selective placement allows fracture behavior to be examined at desired locations such as interfaces and irregularities. Not only can this method of laser machining high aspect ratio channels be used for creating an artificial crack, but it also has applications for fabricating other 3d microstructures. Also, the method developed for laser machining these channels may potentially carry over to other metals pure and composites alike. The laminate fabrication, experiments, and material characterization were performed at Los Alamos National Laboratory at the Center for Integrated NanoTechnologies.

Moreover, the modeling performed in this study shed light on the deformation of stacked layers undergoing plastic deformation. However, the assumptions made do not necessarily capture the true physical phenomena underlying the complex Cu/Nb nano- and micro-systems. Disregarding anisotropy, the interfacial contributions to the materials behavior, and the instantaneous tangent modulus leaves room for improvement in the model. However, modeling the bulk material proves to be valuable in the fundamental design of experiments moving forward to ensure experimental success for in-situ testing. Modeling and simulation using SOLIDWORKS and ANSYS were performed at the University of New Mexico’s Mechanical Engineering Department.

4.2 Suggested Future Work

The following items are suggested for future work:

- Proceed with the in-situ mini cantilever experiments to characterize the fracture behavior of the ARB laminate material.
- Increase the validity of the layered simulation results by removing simplifying assumptions. Incorporate the interfacial effects of the layered structure into the model and perform convergence studies.
- Create a mathematical simulation of the energy transport across the layers as described by each material's applicable energy transport model.
- Perform a statistical analysis on cut results to determine repeatability as affected by layer thickness variance.

Appendix

A1 Pulse Duration Measurement

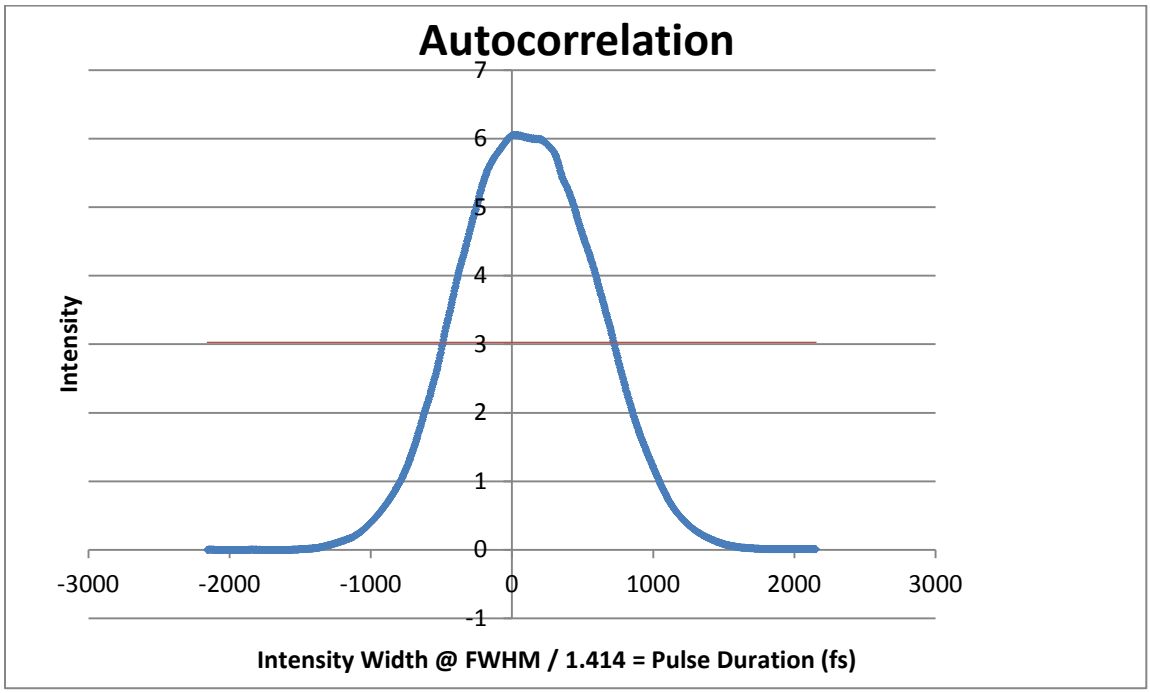

A2. Laser Spot Size Measurements

Knife Edge Power Measurements X-Direction

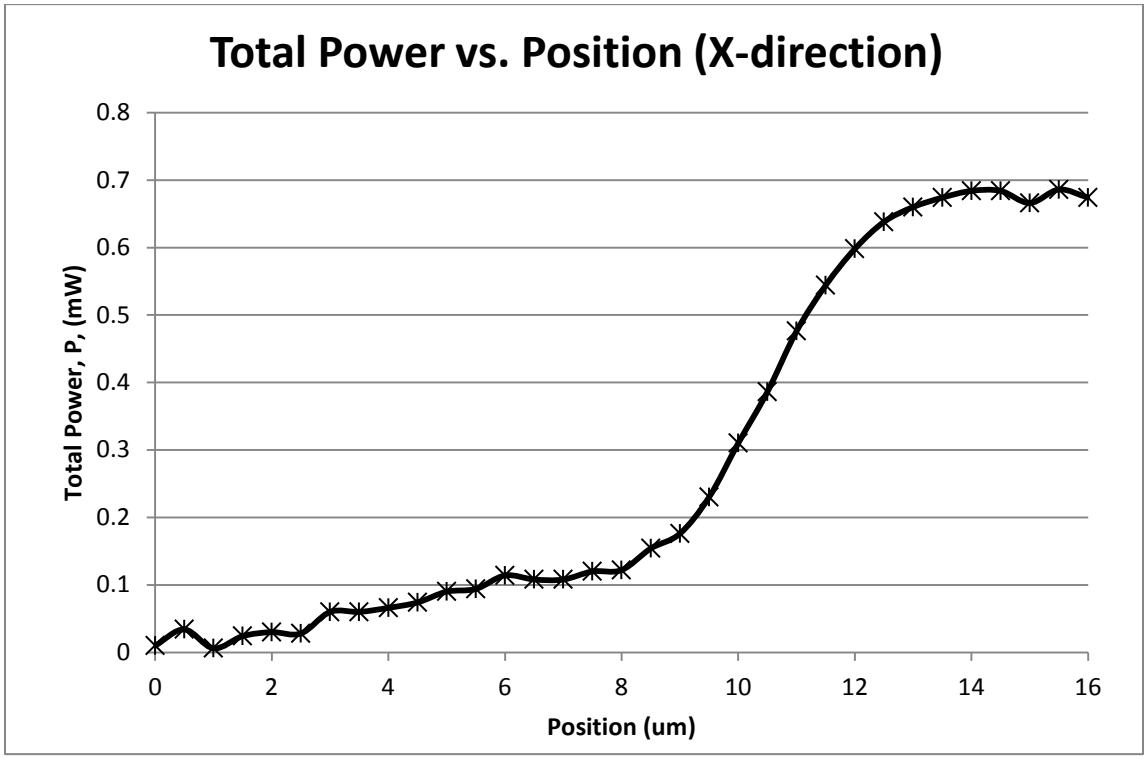

Differentiated Knife Edge Data

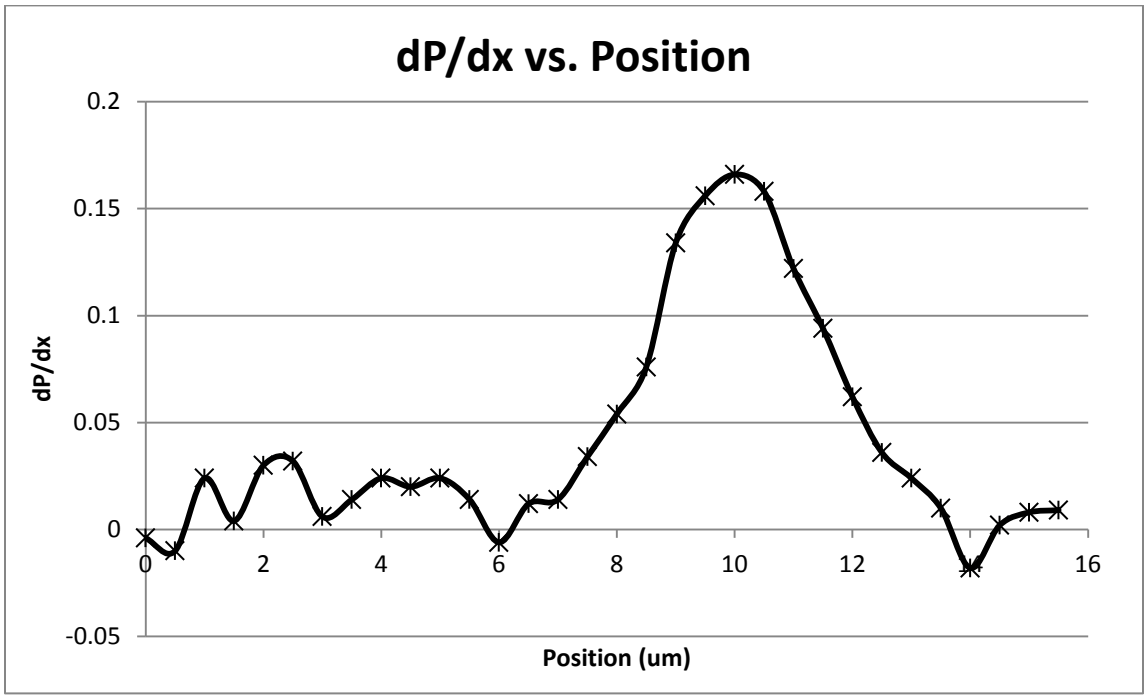

Knife Edge Power Measurements Y-Direction

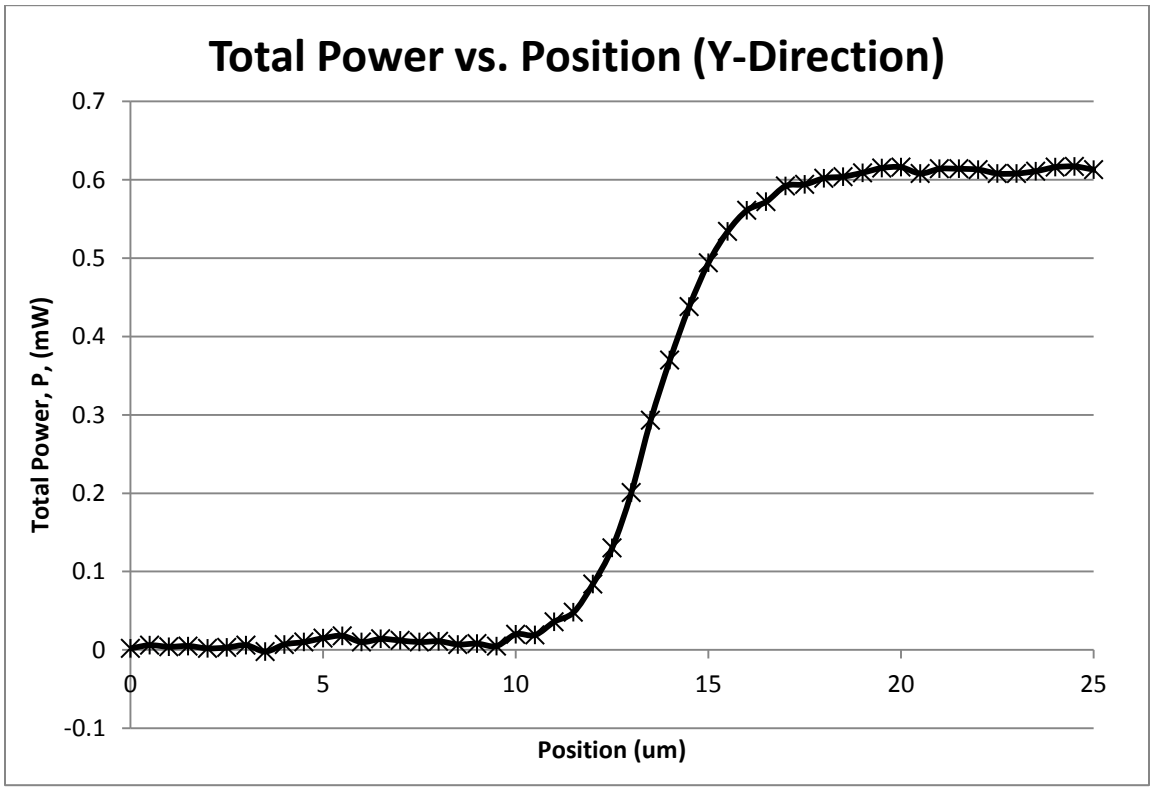

Differentiated Knife Edge Data

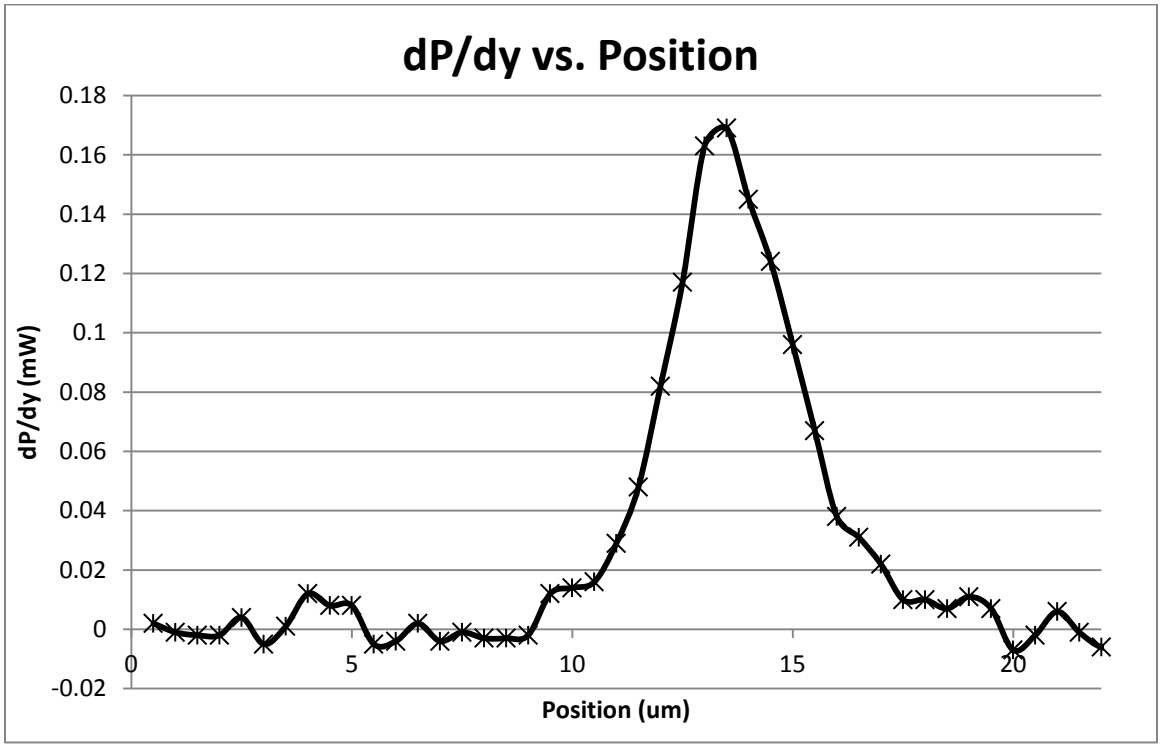

A3. Bulk Model Simulation Validation

1mm Long Pillar	Theoretical	Coarse Simulation	Fine Simulation
Directional Deflection (um)	12.5	12.633	12.623
Element Size (um)	-	20	9
No. of Nodes	-	23441	254352
No. of Elements	-	5000	59248
Error	-	1.06%	0.98%

750um Long Pillar	Theoretical	Coarse Simulation	Fine Simulation
Directional Deflection (um)	16.66	16.843	16.834
Element Size (um)	-	13.6	6.8
No. of Nodes	-	36881	252096
No. of Elements	-	8064	58719
Error	-	1.05%	1.00%

500um Long Pillar	Theoretical	Coarse Simulation	Fine Simulation
Directional Deflection (um)	25	25.265	25.252
Element Size (um)	-	9	4.5
No. of Nodes	-	36881	254352
No. of Elements	-	8064	59248
Error	-	1.06%	1.01%

References

[1] J. Hecht, "Short history of laser developement," *Optical Engineering,* vol. 49, no. 9, pp. 1-23, 2010.

[2] T. Q. Qiu and C. L. Tien, "Femtosecond laser heating of multi-layer metals - I. Analysis," *Int. J. Heat Mass Transfer,* pp. 2789-2797, 1994.

[3] T. Q. Qiu, T. Juhasz, C. Suarez, W. E. Bron and C. L. Tien, "Femtosecond laser heating of multi-layer metals - II. Experiments," *Int. J. Heat Mass Transfer,* vol. 37, no. 17, pp. 2799-2808, 1994.

[4] M. J. Maurer, "Relaxation model for heat conduction in metals," *Journal of Applied Physics,* vol. 40, no. 13, pp. 5123-5130, 1969.

[5] D. D. Joseph and L. Preziosi, "Heat Waves," *Reviews of Modern Physics,* pp. 41-73, 1989.

[6] G. L. Easley, "Relaxation time of electrons," AccessScience McGraw-Hill Education, 2014. [Online]. Available: http://dx.doi.org/10.1036/1097-8542.580300. [Accessed 10 06 2015].

[7] C. Korner and H. W. Bergmann, "The physical defects of the hyperbolic heat conduction equation," *Applied Physics A,* vol. 67, pp. 397-401, 1998.

[8] M. B. Rubin, "Hyperbolic heat conduction and the second law," *Int. J. Ingng. Sci.,* vol. 30, no. 11, pp. 1665-1676, 1992.

[9] S. I. Anisimov, B. L. Kapeliovich and T. L. Perel'man, "Electron emission from metal surfaces exposed to ultrashort laser pulses," *Soviet Physics JETP,* pp. 375-377, 1974.

[10] E. Kannatey-Asibu, Principles of Laser Materials Processing, Hoboken: John Wiley and Sons, Inc., 2009.

[11] T. Q. Qiu and C. L. Tien, "Short-pulse laser heating on metals," *Int. J. Heat Mass Transfer,* vol. 35, no. 3, pp. 719-726, 1992.

[12] T. Q. Qiu and C. L. Tien, "Heat transfer mechanisms during short-pulse laser heating of metals," *J. Heat Transfer,* vol. 115, no. 4, pp. 835-841, 1994.

[13] S. D. Brorson, J. G. Fujimoto and E. P. Ippen, "Femtosecond electronic heat-transfer dynamics in thin gold film," *Phys. Rev. Lett.,* vol. 55, pp. 1962-1965, 1987.

[14] W. S. Fann, R. Storz, H. W. K. Tom and J. Boker, "Electron thermalization in gold," *Phys. Rev. B,* vol. 46, pp. 13 592-13595, 1992.

[15] W. S. Fann, R. Storz, H. W. K. Tom and J. Bokor, "Direct measurement of nonequilibrium electron-energy distributions in sub-picosecond laser-heated gold films," *Phys. Rev. Lett.,* vol. 68, no. 18, pp. 2834-2837, 1992.

[16] G. Veshapidze, M. L. Trachy, M. H. Shah and B. D. DePaola, "Reducing the uncertainty in laser beam size measurement with a scanning edge method," *Applied Optics,* vol. 45, no. 32, pp. 8197-8199, 2006.

[17] A. E. Siegman, "How to (maybe) measure laser beam quality," *Diode Pumped Solid State Lasers: Applications and Issues, M. Dowley, ed.,,* vol. 17 of OSA Trends in Optics and Photonics, pp. 184-199, 1998.

[18] J. Magnes, D. Odera, J. Hartke, M. Fountain, L. Florence and V. Davis, "Quantitative and Qualitative Study of Beam Visualization Techniques," arXiv preprint physics/0605102, West Point, NY, 2006.

[19] J. Byskov-Nielsen, "Short-pulse laser ablation of metals: Fundamentals and applications for micro-mechanical interlocking. PhD Diss. Department of physics and Astronomy," University of Aarhus, Aarhus, Denmark, 2010.

[20] N. Hänel, M. Stolze, T. Herrmann and J. A. Lhuillier, "Fundamental investigations of ps-laser burst-mode on common metals for an enhanced ablation process," in *Proc. SPIE 9351, Laser-based Micro- and Nanoprocessing IX, 93510E*, San Fransisco, California, 2015.

[21] P. T. Mannion, J. Magee, E. Coyne, G. M. O'Connor and T. J. Glynn, "The effect of damage accumulation behaviour on ablation thresholds and damage morphology in ultrafast laser micro-machining of common metals in air," *Applied Surface Science,* vol. 233, no. 1-4, pp. 275-287, 2004.

[22] Y. Jee, M. F. Becker and R. M. Walser, "Laser-induced damage on single-crystal metal surfaces," *Journal of the Optical Society of America B,* vol. 5, no. 3, pp. 648-659, 1988.

[23] A. Y. Vorobyev and C. Guo, "Reflection of femtosecond laser light in multipulse ablation of metals," *Journal of Applied Physics,* vol. 110, no. 4, pp. 043102 (2-10), 2011.

[24] B. Neuenschwander, B. Jaeggi, M. Schmind, A. Dommann, A. Neels, T. Bandi and G. Hennig, "Factors controlling the incubation in the aplication of ps laser pulses on copper and iron surfaces," in *Laser Applications in Microelectronic and Optoelectronic Manufacturing (LAMOM) XVIII*, San Fransicso, California, 2013.

[25] S. E. Kirkwood, A. C. Van Popta, Y. Y. Tsui and R. Fedosejevs, "Single and multiple shot near-infrared femtosecond laser pulse ablation thresholds of copper," *Applied Physics A,* vol. 81, no. 4, pp. 729-735, 2005.

[26] W. Mook, J. K. Baldwin, M. M. Ricardo and N. A. Mara, "SEM in situ MiniCantilever Beam Bending of U-10Mo/Zr/Al Fuel Elements," LANL, Los Alamos, NM, 2014.

[27] D. Kiener, C. Motz, M. Rester, M. Jenko and G. Dehm, "FIB damage of Cu and possible consequences for miniaturized mechanical tests," *Material Science & Engineering A,* vol. 459, no. 1-2, pp. 262-272, 2007.

[28] J. S. Carpenter, S. C. Vogel, J. E. LeDonne, D. L. Hammnon, I. J. Beyerlein and N. A. Mara, "Bulk texture evlolution of Cu-Nb nanolemellar composites during accumulative roll bonding," *Acta Materialia,* vol. 60, no. 4, pp. 1576-1586, 2012.

[29] J. Cheng, L. Chang-Sheng, S. Shang, D. Liu and W. Perrie, "A review of ultrafast laser materials micromachining," *Optics & Laser Technology,* vol. 46, pp. 88-102, 2013.

[30] S. Nolte, C. Momma, H. Jacobs, A. Tunnermann, B. N. Chichkov, B. Wellegehausen and H. Welling, "Ablation of metals by ultrashort laser pulses," *J. Opt. Soc. Am. B.,* vol. 14, no. 10, pp. 2716-2722, 1997.

[31] M. Gedeon, "Stress-Strain concepts revisited - part 2," *Materion Brush Performance Alloys Technical Tidbits,* pp. 1-2, October 2012.

[32] T. Nizolek, I. J. Beyerlein, N. A. Mara, J. Y. Avallone and T. M. Pollock, "Tensile Behaviour and flow stress anisotropy of accumulative roll bonded Cu-Nb nanolaminates," *Applied Physics Letters,* vol. 108, no. 5, pp. 1-4,

2016.

[33] D. Roylance, "Stress-Strain Curves," 23 August 2001. [Online]. Available: http://ocw.mit.edu/courses/materials-science-and-engineering/3-11-mechanics-of-materials-fall-1999/modules/ss.pdf. [Accessed 07 January 2016].

[34] ASM International, The Atlas of Stress-Strain Curves 2nd Ed., Materials Park: ASM International, 2002.

[35] A. G. Imgram, M. W. Mallett, B. G. Koehl, E. S. Bartlett and H. R. Ogden, "Notch Sensitivity of Refractory Metals," Battelle Memorial Inst., Ohio, 1962.

[36] D. Roylance, "Massuchusetts Institute of Technology," 2008. [Online]. Available: http://web.mit.edu/course/3/3.225/book.pdf. [Accessed 22 2 2016].

[37] The Engineering ToolBox, "The Engineering ToolBox," [Online]. Available: http://www.engineeringtoolbox.com. [Accessed 01 03 2016].